A Discrete-Time Domain Modeling of LLC Resonant Converter Considering the Nonlinearity of Voltage-Controlled Oscillator

Yuecheng Zhang
College of Automation Engineering
Nanjing University of Aeronautics and Astronautics
Nanjing, China
zhangyc@nuaa.edu.cn

Xinbo Ruan
College of Automation Engineering
Nanjing University of Aeronautics and Astronautics
Nanjing, China
ruanxb@nuaa.edu.cn

Ying Li
Department of Electrical and Electronic Engineering
University of Nottingham
Nottingham, UK
Ying.Li1@nottingham.ac.uk

***Abstract*—The LLC resonant converter, featured with soft switching realization, magnetic components simplicity, high conversion efficiency, high-power density and low EMI noise, has been widely used in diverse fields. Voltage-controlled oscillator (VCO), which shows strong nonlinear characteristics, plays a crucial role in output voltage regulating of the LLC resonant converter. However, in small-signal modeling for LLC resonant converter, VCO is usually treated as a constant gain, which will relegate the model accuracy especially in the high-frequency region. In this paper, an accurate small-signal model that can reflect the nonlinearity of VCO is proposed. The discrete-time small-signal model of the power stage is also deduced by exploiting the half-cycle symmetry for simplifying the derivation. Then the transfer function from the modulation signal to output voltage of the LLC resonant converter is developed. Finally, the simulation results verify the accuracy of the proposed model.**

Keywords—LLC resonant converter, voltage-controlled oscillator (VCO), discrete-time model

I. Introduction

LLC resonant converter exhibits the advantages of soft switching realization, magnetic components simplicity, high conversion efficiency, high-power density and low EMI noise. Therefore, LLC resonant converter has been widely used in diverse fields, including aerospace, data center power supply, electric vehicle chargers and solar array simulator in photovoltaic application [1]–[4]. In order to design an optimal controller and analyze its stability, it is desirable to derive an accurate small-signal model for LLC resonant converter.

For switching converters, the most widely used small-signal modeling method is the averaging method [5], which takes the periodic average of the state variables and ignores the influence of the switching ripple. The state variables in resonant tank of resonant converters do not have dc components, but contain strong switching frequency component and its harmonics, so the averaging method is not applicable to resonant converters.

Based on fundamental harmonic approximation and the principle of harmonic balance, the extended describing function (EDF) method establishes the small-signal model of resonant converters in state space representation and derives the corresponding equivalent circuit [6], [7]. Using the EDF method, the small-signal model of LLC resonant converter was developed in [8]. This model shows good accuracy in the region where the switching frequency is close to the resonant frequency. However, when the switching frequency deviates from the resonant frequency, the resonant tank of LLC resonant converter hardly behaves as an ideal band-pass filter and more harmonic components are involved in energy transfer. To improve the accuracy of the small-signal model, more harmonic components should be incorporated in modeling. Besides, voltage-controlled oscillator (VCO), which shows strong nonlinear characteristics, plays a crucial role in frequency-controlled LLC resonant converter and should be taken into consideration as well. The frequency domain small-signal modeling for LLC resonant converter based on describing function method, which captures the influence of all harmonics and the nonlinearity of VCO, was given in [9]. This model is very accurate, however, its derivations and results are complicated, which provides limited guidance for controller design.

The discrete-time modeling method [10]–[12] focuses on the accurate modeling of the power stage with consideration of all harmonics. However, there is no extension to the popular LLC resonant converter using this method [9]. In this paper, a discrete-time small-signal model of LLC resonant converter is derived step by step. The half-cycle symmetry characteristic of the power stage is exploited to simplify the analysis. In the conventional discrete-time modeling for resonant converters, VCO is usually treated as a constant gain, which relegates the accuracy of the model. To improve the accuracy of the model, this paper will analyze the principle of VCO in detail and establish its accurate small-signal model. Combining VCO with the power stage, the transfer function from the modulation signal to output voltage of LLC resonant converter is developed for the design of controller and stability analysis.

This paper is organized as follows. In Section II, the discrete-time modeling of the power stage of LLC resonant converter is derived in detail. Section III establishes the accuracy small-signal model of VCO. Section IV verifies the accuracy of the proposed model by simulation. Finally, Section V concludes this paper.

II. Discrete-Time Modeling of the Power Stage of LLC Resonant Converter

Fig. 1 shows the schematic diagram of LLC resonant converter. The power stage consists of an inverter, a resonant tank, a rectifier and an output filter. In Fig. 1, V_{in} is the input voltage, L_r and C_r are the resonant inductor and the resonant capacitor whose resonant frequency is denoted as f_r, L_m is the magnetizing inductor, T_r is the transformer whose turn ratio is N:1, C_o is the output capacitor and R_{Ld} is the load resistance. v_{AB} is the inverter output voltage, i_{Lr} and i_{Lm} are the respective currents going through L_r and L_m, v_{Cr} is the voltage of C_r, v_p and i_p are the respective primary voltage and primary current of T_r and i_R is the rectified current. H_v is the feedback coefficient of the output voltage v_o, v_{fb} is the feedback signal of v_o, V_{ref} is the voltage reference, G_c is the feedback controller, v_m is the modulation signal and v_{gs} is the driving signal.

In this section, the discrete-time small-signal model of the power stage of LLC resonant converter will be deduced. In the following derivation, all switching devices, inductors and capacitors are ideal.

A. State Space Equations

In the power stage, i_{Lr}, i_{Lm}, v_{Cr} and v_o are chosen as state variables in the analysis. The state vector $\boldsymbol{x}(t)$ is defined as

$$\boldsymbol{x}(t) = \begin{bmatrix} i_{Lr} - i_{Lm} & i_{Lm} & v_{Cr} & v_o \end{bmatrix}^{T} \tag{1}$$

It should be noted that the difference between i_{Lr} and i_{Lm} is taken as the first state variable in (1) for the convenience of the following derivation.

The typical waveforms of full-bridge LLC resonant converter are shown in Fig. 2, where Q_{gs_p} is the driving signal for the positive half period and t_s is the switching period. The kth ($k = 0, 1, 2, ...$) sampling period, denoted as t_{sa_k}, is

$$t_{sa\_k} = t_{k+1} - t_k \tag{2}$$

where t_k is the sampling instant, i.e. the beginning instant of t_{sa_k}, t_{k+1} is the ending instant of t_{sa_k}, t_k+t_{ak} is the switching instant from mode S_1 to mode S_2. The first mode occurs at the sampling period is defined as mode S_1 and the second is defined as mode S_2.

As seen in Fig. 2, the state variables exhibit half-cycle symmetry, where v_o is even symmetry and the other variables are odd symmetry. Therefore, only the positive half period of the converter needs to be analyzed. The equivalent circuits of the positive half period are shown in Fig. 3.

Region 1 ($f_s < f_r$): in mode S_1, L_r resonates with C_r and the voltage of L_m is clamped at Nv_o. The equivalent circuit during the interval $t_k < t < t_k+t_{ak}$ is shown in Fig. 3(a). At $t = t_k+t_{ak}$, i_{Lr} and i_{Lm} are equal. In mode S_2, L_m in series with L_r resonate with C_r and the output is separated from the transformer. The equivalent circuit during the interval $t_k+t_{ak} < t < t_{k+1}$ is shown in Fig. 3(b).

Region 2 ($f_s > f_r$): in mode S_1, L_r resonates with C_r and the voltage of L_m is clamped at $-Nv_o$. The equivalent circuit during the interval $t_k < t < t_k+t_{ak}$ is shown in Fig. 3(c). At $t = t_k+t_{ak}$, i_{Lr} and i_{Lm} are equal. Then the voltage of L_m is clamped at Nv_o. The equivalent circuit during the interval $t_k+t_{ak} < t < t_{k+1}$ is shown in Fig. 3(a).

Based on the symmetry characteristic of LLC resonant converter, the state variables can be substituted as follows

$$\boldsymbol{x}_s(t) = \begin{cases} \boldsymbol{x}(t) & \text{positive half period} \\ \mathbf{M}_r \boldsymbol{x}(t) + \mathbf{M}_v & \text{negative half period} \end{cases} \tag{3}$$

where the matrices $\mathbf{M}_r$ and $\mathbf{M}_v$ are determined by the half-cycle symmetry of the state variables

$$\mathbf{M}_r = \mathrm{diag}[-1, -1, -1, 1] \tag{4}$$

$$\mathbf{M}_v = \begin{cases} \begin{bmatrix} 0 & 0 & 0 & 0 \end{bmatrix}^T & \text{full-bridge} \\ \begin{bmatrix} 0 & 0 & V_{in} & 0 \end{bmatrix}^T & \text{half-bridge} \end{cases} \tag{5}$$

The positive half period of $\boldsymbol{x}_s(t)$ is the same as $\boldsymbol{x}(t)$, while the negative half period is symmetrically transformed with respect to $\boldsymbol{x}(t)$. The waveforms after transformation are shown in Fig. 4, where i_{Lr_s}, i_{Lm_s}, v_{Cr_s} and v_{o_s} are the waveforms of i_{Lr}, i_{Lm}, v_{Cr} and v_o after transformation, respectively.

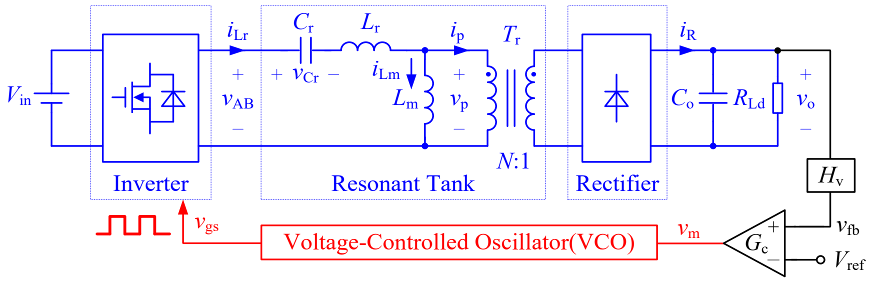

Fig. 1. The schematic diagram of LLC resonant converter.

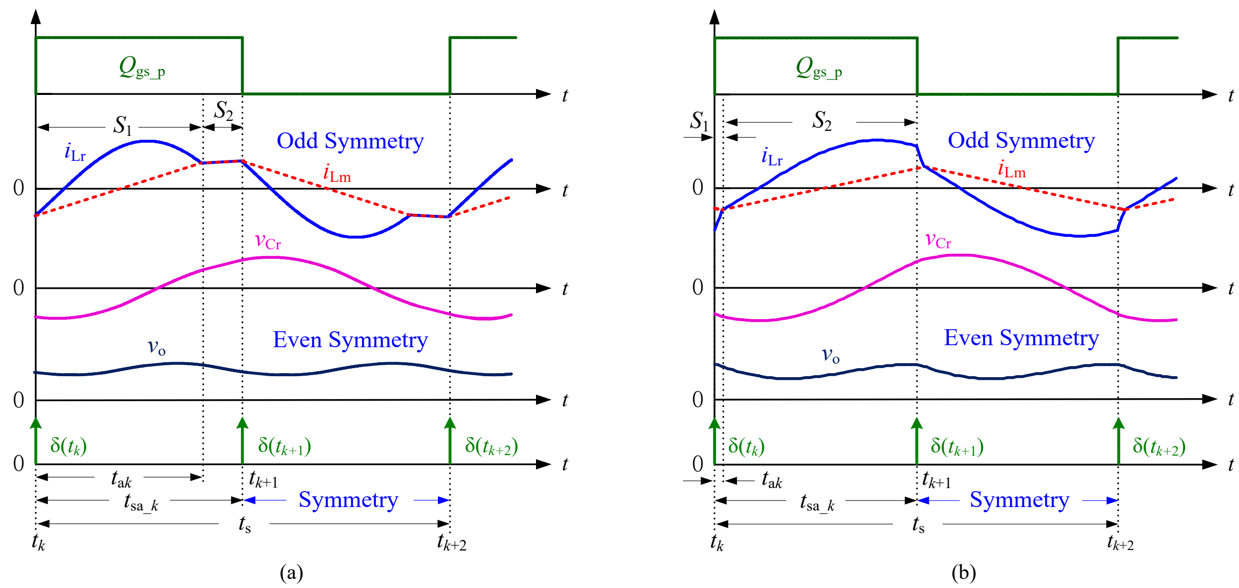

Fig. 2. Typical waveforms of the full-bridge LLC resonant converter. (a) $f_s < f_r$; (b) $f_s > f_r$.

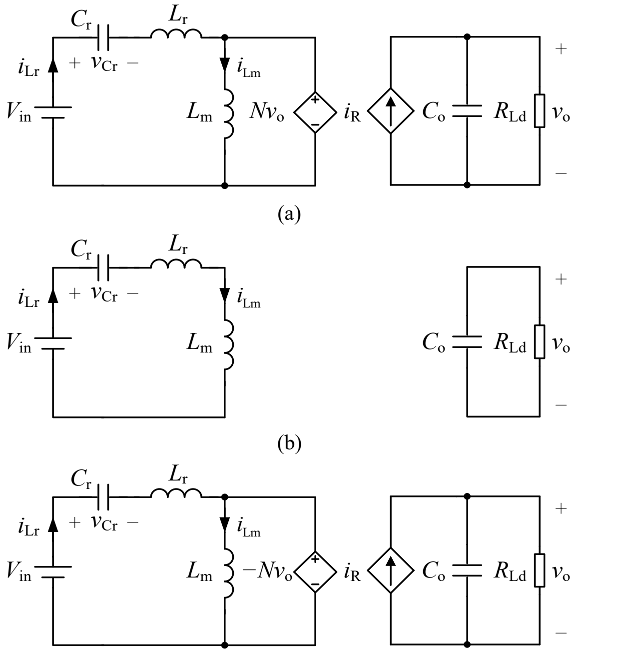

Fig. 3. Equivalent circuits of the positive half period. (a) L_r resonates with C_r, $v_p = Nv_o$; (b) L_m in series with L_r resonate with C_r; (c) L_r resonates with C_r, $v_p = -Nv_o$.

According to Fig. 2 and Fig. 3, the state space equations of LLC resonant converter in mode S_1 and mode S_2 are respectively obtained as

$$\begin{cases} \dfrac{d\boldsymbol{x}_s(t)}{dt} = \mathbf{A}_1\boldsymbol{x}_s(t) + \mathbf{B}_1 V_{in} \\ v_o(t) = \mathbf{C}\boldsymbol{x}_s(t) \end{cases} \quad S_1 : t_k < t < t_k + t_{ak} \tag{6}$$

$$\begin{cases} \dfrac{d\boldsymbol{x}_s(t)}{dt} = \mathbf{A}_2\boldsymbol{x}_s(t) + \mathbf{B}_2 V_{in} \\ v_o(t) = \mathbf{C}\boldsymbol{x}_s(t) \end{cases} \quad S_2 : t_k + t_{ak} \le t < t_{k+1} \tag{7}$$

where $\mathbf{A}_i$ and $\mathbf{B}_i$ represent the state matrices of mode S_i respectively, i = 1,2 and $\mathbf{C}$ is the output matrix. Expressions of the coefficient matrices in the state space equations are listed in Table I.

As shown in Fig. 4, $\boldsymbol{x}_s(t)$ obtains the property of even half-cycle symmetry after transformation with respect to $\boldsymbol{x}(t)$. However, the transformation destroys the continuity at the sampling instants for the odd symmetry variables in $\boldsymbol{x}(t)$. At the sampling instants, the left limit and the right limit of $\boldsymbol{x}_s(t)$ satisfy

$$\boldsymbol{x}_s(t_k^+) = \mathbf{M}_r \boldsymbol{x}_s(t_k^-) + \mathbf{M}_v \tag{8}$$

B. Difference Equations

The solutions of (6) and (7) are shown in (9), where the matrix function $\mathbf{E}_i(t)$ is expressed as

$$\mathbf{E}_i(t) = \int_0^t e^{\mathbf{A}_i \tau} d\tau \quad i = 1,2 \tag{10}$$

To simplify the analysis, $\boldsymbol{x}_s(t_k)$ is defined to be equal to its

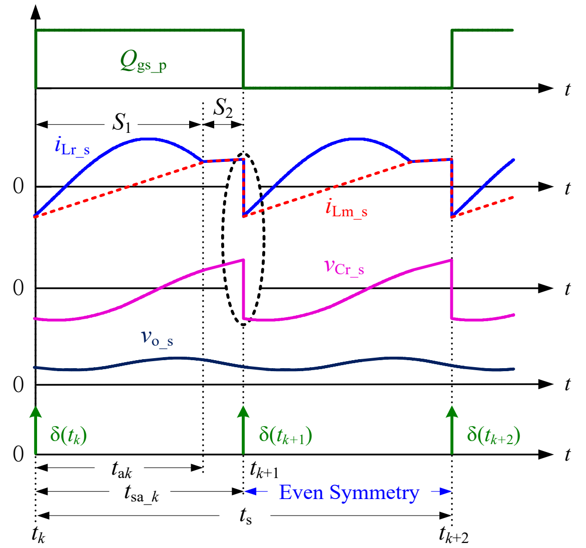

Fig. 4. Typical waveforms after symmetry transform ($f_s < f_r$).

right limit, i.e.,

$$\boldsymbol{x}_s(t_k) = \boldsymbol{x}_s(t_k^+) \tag{11}$$

Substituting (8) and (11) into (9), the expressions of $\boldsymbol{x}_s(t)$ at t_k+t_{ak} and t_{k+1} can be obtained as

$$\boldsymbol{x}_s(t_k + t_{ak}) = e^{\mathbf{A}_1 t_{ak}} \boldsymbol{x}_s(t_k) + \mathbf{E}_1(t_{ak})\mathbf{B}_1 V_{in} \tag{12}$$

$$\begin{aligned} &\mathbf{M}_r \boldsymbol{x}_s(t_{k+1}) + \mathbf{M}_v \\ &= e^{\mathbf{A}_2(t_{k+1} - t_k - t_{ak})} \boldsymbol{x}_s(t_k + t_{ak}) + \mathbf{E}_2(t_{k+1} - t_k - t_{ak})\mathbf{B}_2 V_{in} \end{aligned} \tag{13}$$

Putting (12) into (13), we have

$$\begin{aligned} &\mathbf{M}_r \boldsymbol{x}_s(t_{k+1}) + \mathbf{M}_v \\ &= e^{\mathbf{A}_2(t_{k+1} - t_k - t_{ak})} e^{\mathbf{A}_1 t_{ak}} \boldsymbol{x}_s(t_k) + e^{\mathbf{A}_2(t_{k+1} - t_k - t_{ak})} \mathbf{E}_1(t_{ak})\mathbf{B}_1 V_{in} \\ &\quad + \mathbf{E}_2(t_{k+1} - t_k - t_{ak})\mathbf{B}_2 V_{in} \end{aligned} \tag{14}$$

According to (6) and (11), the output voltage at the sampling instants can be written as

$$v_o(t_k) = \mathbf{C}\boldsymbol{x}_s(t_k) \tag{15}$$

C. Steady-State Operation Point Calculation

At the steady-state operation of the converter, T_k is defined as the start instant of the sampling period, i.e. the sampling instant, T_{sa} represents the sampling period and T_k+T_a is the switching instant from mode S_1 to mode S_2. T_k and T_{sa} are related to the switching period T_s as follows

$$T_k = \frac{k}{2} T_s \tag{16}$$

$$T_{sa} = \frac{1}{2} T_s \tag{17}$$

Moreover, the steady-state values of $\boldsymbol{x}_s(t)$ are equal at every sampling instants and the mode switching instants, i.e.,

$$\boldsymbol{X}_s(T_{k+1}) = \boldsymbol{X}_s(T_k) = \boldsymbol{X}_s(0) \tag{18}$$

$$\boldsymbol{x}_s(t) = \begin{cases} e^{\mathbf{A}_1(t - t_k)} \boldsymbol{x}_s(t_k^+) + \mathbf{E}_1(t - t_k)\mathbf{B}_1 V_{in} & S_1 : t_k < t < t_k + t_{ak} \\ e^{\mathbf{A}_2(t - t_k - t_{ak})} \boldsymbol{x}_s(t_k + t_{ak}) + \mathbf{E}_2(t - t_k - t_{ak})\mathbf{B}_2 V_{in} & S_2 : t_k + t_{ak} \le t < t_{k+1} \end{cases} \tag{9}$$

TABLE I. COEFFICIENT MATRICES OF STATE SPACE EQUATIONS

Region	$\mathbf{A}_1$	$\mathbf{A}_2$	$\mathbf{B}_1$	$\mathbf{B}_2$	$\mathbf{C}$
$f_s < f_r$	$\begin{bmatrix} 0 & 0 & -\frac{1}{L_r} & -\frac{N}{L_r}-\frac{N}{L_m} \\ 0 & 0 & 0 & \frac{N}{L_m} \\ \frac{1}{C_r} & \frac{1}{C_r} & 0 & 0 \\ \frac{N}{C_o} & 0 & 0 & -\frac{1}{R_{Ld}C_o} \end{bmatrix}$	$\begin{bmatrix} 0 & 0 & 0 & 0 \\ 0 & 0 & -\frac{1}{L_r+L_m} & 0 \\ \frac{1}{C_r} & \frac{1}{C_r} & 0 & 0 \\ 0 & 0 & 0 & -\frac{1}{R_{Ld}C_o} \end{bmatrix}$	$\begin{bmatrix} \frac{1}{L_r} \\ 0 \\ 0 \\ 0 \end{bmatrix}$	$\begin{bmatrix} 0 \\ \frac{1}{L_r+L_m} \\ 0 \\ 0 \end{bmatrix}$	$\begin{bmatrix} 0 & 0 & 0 & 1 \end{bmatrix}$
$f_s > f_r$	$\begin{bmatrix} 0 & 0 & -\frac{1}{L_r} & \frac{N}{L_r}+\frac{N}{L_m} \\ 0 & 0 & 0 & -\frac{N}{L_m} \\ \frac{1}{C_r} & \frac{1}{C_r} & 0 & 0 \\ -\frac{N}{C_o} & 0 & 0 & -\frac{1}{R_{Ld}C_o} \end{bmatrix}$	$\begin{bmatrix} 0 & 0 & -\frac{1}{L_r} & -\frac{N}{L_r}-\frac{N}{L_m} \\ 0 & 0 & 0 & \frac{N}{L_m} \\ \frac{1}{C_r} & \frac{1}{C_r} & 0 & 0 \\ \frac{N}{C_o} & 0 & 0 & -\frac{1}{R_{Ld}C_o} \end{bmatrix}$	$\begin{bmatrix} \frac{1}{L_r} \\ 0 \\ 0 \\ 0 \end{bmatrix}$	$\begin{bmatrix} \frac{1}{L_r} \\ 0 \\ 0 \\ 0 \end{bmatrix}$	$\begin{bmatrix} 0 & 0 & 0 & 1 \end{bmatrix}$

$$\boldsymbol{X}_s\left(T_k+T_a\right)=\boldsymbol{X}_s\left(T_a\right) \tag{19}$$

Substituting (18) into (14) yields

$$\boldsymbol{X}_s(0)=\left(\mathbf{M}_r-\boldsymbol{\varphi}_2\boldsymbol{\varphi}_1\right)^{-1}\left(\boldsymbol{\varphi}_2\boldsymbol{\psi}_1\mathbf{B}_1V_{in}+\boldsymbol{\psi}_2\mathbf{B}_2V_{in}-\mathbf{M}_v\right) \tag{20}$$

where

$$\boldsymbol{\varphi}_1=e^{\mathbf{A}_1T_a} \tag{21a}$$

$$\boldsymbol{\varphi}_2=e^{\mathbf{A}_2\left(T_{sa}-T_a\right)} \tag{21b}$$

$$\boldsymbol{\psi}_1=\mathbf{E}_1\left(T_a\right) \tag{21c}$$

$$\boldsymbol{\psi}_2=\mathbf{E}_2\left(T_{sa}-T_a\right) \tag{21d}$$

Substituting (18) and (19) into (12), the steady-state value of $\boldsymbol{x}_s(t)$ at the mode switching instants can be obtained as

$$\boldsymbol{X}_s\left(T_a\right)=\boldsymbol{\varphi}_1\boldsymbol{X}_s\left(0\right)+\boldsymbol{\psi}_1\mathbf{B}_1V_{in} \tag{22}$$

Although the steady-state equations (20), (21) and (22) are obtained, it is not enough to calculate the steady-state point. There still exists an unknown variable T_a, which can be determined by the boundary condition

$$i_{Lr}\left(T_a\right)-i_{Lm}\left(T_a\right)=\mathbf{R}_1\boldsymbol{X}_s\left(T_a\right)=0 \tag{23}$$

where $\mathbf{R}_1=\begin{bmatrix}1 & 0 & 0 & 0\end{bmatrix}$.

Due to the complex resonance in the LLC resonant converter, it is difficult to calculate the analytical solution of (23). Therefore, T_a is computed iteratively and then substituted into (20), (21) and (22) to determine the steady-state point.

D. Small-Signal Perturbation and Linearization

The sampling instants, mode switching instants, state variables and the output variable can be expressed as the steady-state point plus the small-signal perturbation

$$t_k=T_k+\hat{t}_k \tag{24a}$$

$$t_k+t_{ak}=T_k+T_a+\hat{t}_k+\hat{t}_{ak} \tag{24b}$$

$$\boldsymbol{x}_s\left(t\right)=\boldsymbol{X}_s\left(t\right)+\hat{\boldsymbol{x}}_s\left(t\right) \tag{24c}$$

$$v_o\left(t\right)=V_o\left(t\right)+\hat{v}_o\left(t\right) \tag{24d}$$

Taking the zero-order Talyor polynomial of (24c) and (24d) at the sampling instants, we have

$$\boldsymbol{x}_s\left(t_k\right)=\boldsymbol{X}_s\left(T_k\right)+\hat{\boldsymbol{x}}_s\left(T_k\right) \tag{25}$$

$$v_o\left(t_k\right)=V_o\left(T_k\right)+\hat{v}_o\left(T_k\right) \tag{26}$$

Substituting (24) and (25) into (14), eliminating the steady-state values and ignoring the high order ac terms, the following difference equation can be obtained

$$\begin{aligned}\mathbf{M}_r\hat{\boldsymbol{x}}_s\left(T_{k+1}\right)&=\boldsymbol{\varphi}_2\boldsymbol{\varphi}_1\hat{\boldsymbol{x}}_s\left(T_k\right)+\boldsymbol{\varphi}_2\boldsymbol{X}_s'\left(T_a^+\right)\hat{t}_{sa\_k}\\&\quad+\boldsymbol{\varphi}_2\left[\boldsymbol{X}_s'\left(T_a^-\right)-\boldsymbol{X}_s'\left(T_a^+\right)\right]\hat{t}_{ak}\end{aligned} \tag{27}$$

where $\hat{t}_{sa\_k}=\hat{t}_{k+1}-\hat{t}_k$, $\boldsymbol{X}_s'\left(T_a^-\right)$ and $\boldsymbol{X}_s'\left(T_a^+\right)$ are the respective left derivative and right derivative of $\boldsymbol{x}_s(t)$ at T_a in the steady-state operation, which can be written as

$$\boldsymbol{X}_s'\left(T_a^-\right)=\mathbf{A}_1\boldsymbol{X}_s\left(T_a\right)+\mathbf{B}_1V_{in} \tag{28}$$

$$\boldsymbol{X}_s'\left(T_a^+\right)=\mathbf{A}_2\boldsymbol{X}_s\left(T_a\right)+\mathbf{B}_2V_{in} \tag{29}$$

In the process of linearization, on the assumption of the small-signal perturbation, the matrix functions in (14) can be approximated as

$$e^{\mathbf{A}_i\left(T+\hat{t}\right)}\approx e^{\mathbf{A}_iT}\left(\mathbf{I}+\mathbf{A}_i\hat{t}\right)\quad i=1,2 \tag{30}$$

$$\mathbf{E}_i\left(T+\hat{t}\right)=\int_0^{T+\hat{t}}e^{\mathbf{A}_i\tau}d\tau\approx\mathbf{E}_i\left(T\right)+e^{\mathbf{A}_iT}\hat{t}\quad i=1,2 \tag{31}$$

where T is the steady-state value, $\hat{t}$ is the small-signal perturbation and $\mathbf{I}$ is the unit matrix.

Furthermore, according to Fig. 2, at $t=t_k+t_{ak}$, i_{Lr} and i_{Lm} are equal. The constraint equation can be written as

$$i_{Lr}\left(t_k+t_{ak}\right)-i_{Lm}\left(t_k+t_{ak}\right)=\mathbf{R}_1\boldsymbol{x}_s\left(t_k+t_{ak}\right)=0 \tag{32}$$

Substituting (12) into (32), after small-signal perturbation and linearization, we have

$$\mathbf{R}_1\boldsymbol{\varphi}_1\hat{\boldsymbol{x}}_s\left(T_k\right)+\mathbf{R}_1\boldsymbol{\varphi}_1\left[\mathbf{A}_1\boldsymbol{X}_s\left(0\right)+\mathbf{B}_1V_{in}\right]\hat{t}_{ak}=0 \tag{33}$$

Substituting (33) into (27), eliminating the small-signal component $\hat{t}_{ak}$, we obtain

$$\mathbf{M}_r\hat{\boldsymbol{x}}_s\left(T_{k+1}\right)=\mathbf{\Phi}\hat{\boldsymbol{x}}_s\left(T_k\right)+\mathbf{\Psi}\hat{t}_{sa\_k} \tag{34}$$

where

$$\boldsymbol{\Phi} = \boldsymbol{\varphi}_2\boldsymbol{\varphi}_1 + \boldsymbol{\varphi}_2\left[\boldsymbol{X}_{\mathrm{s}}'\left(T_{\mathrm{a}}^{-}\right) - \boldsymbol{X}_{\mathrm{s}}'\left(T_{\mathrm{a}}^{+}\right)\right]\boldsymbol{K} \tag{35a}$$

$$\boldsymbol{\Psi} = \boldsymbol{\varphi}_2\boldsymbol{X}_{\mathrm{s}}'\left(T_{\mathrm{a}}^{+}\right) \tag{35b}$$

$$\boldsymbol{K} = -\frac{\mathbf{R}_1\boldsymbol{\varphi}_1}{\mathbf{R}_1\boldsymbol{\varphi}_1\left[\mathbf{A}_1\boldsymbol{X}_{\mathrm{s}}(0) + \mathbf{B}_1V_{\mathrm{in}}\right]} \tag{35c}$$

The frequency of t_{sa_k} can be expressed as

$$\begin{aligned} f_{\mathrm{sa}\_k} &= f_{\mathrm{sa}} + \hat{f}_{\mathrm{sa}\_k} = 2f_{\mathrm{s}} + \hat{f}_{\mathrm{sa}\_k} \\ &= \frac{1}{t_{\mathrm{sa}\_k}} = \frac{1}{T_{\mathrm{sa}} + \hat{t}_{\mathrm{sa}\_k}} \approx \frac{1}{T_{\mathrm{sa}}} - \frac{1}{T_{\mathrm{sa}}^{\,2}}\hat{t}_{\mathrm{sa}\_k} \end{aligned} \tag{36}$$

which indicates

$$\hat{f}_{\mathrm{sa}\_k} = -\frac{1}{T_{\mathrm{sa}}^{\,2}}\hat{t}_{\mathrm{sa}\_k} \tag{37}$$

Assume that VCO is a constant gain, both the period and frequency can be treated as continuous time domain functions. The continuous sampling frequency, denoted as $f_{\mathrm{sa\_c}}$, satisfies

$$\hat{f}_{\mathrm{sa\_c}}(t) = 2K_{\mathrm{VCO}}\hat{v}_{\mathrm{m}}(t) \tag{38}$$

where K_{VCO} is defined as

$$K_{\mathrm{VCO}} = \frac{f_{\mathrm{s}}}{V_{\mathrm{m}}} = \frac{f_{\mathrm{sa}}}{2V_{\mathrm{m}}} = \frac{1}{2V_{\mathrm{m}}T_{\mathrm{sa}}} \tag{39}$$

Moreover, the small-signal component $\hat{f}_{\mathrm{sa}\_k}$ can be written as

$$\hat{f}_{\mathrm{sa}\_k} = \hat{f}_{\mathrm{sa\_c}}\left(T_{k+1}\right) \tag{40}$$

where the sampling instants will be explained in Section III.

Substituting (37) and (40) into (34), the linearized difference equation of $\hat{\boldsymbol{x}}_{\mathrm{s}}$ and $\hat{f}_{\mathrm{sa\_c}}$ is

$$\mathbf{M}_{\mathrm{r}}\hat{\boldsymbol{x}}_{\mathrm{s}}\left(T_{k+1}\right) = \boldsymbol{\Phi}\hat{\boldsymbol{x}}_{\mathrm{s}}\left(T_k\right) - T_{\mathrm{sa}}^{\,2}\boldsymbol{\Psi}\hat{f}_{\mathrm{sa\_c}}\left(T_{k+1}\right) \tag{41}$$

Applying small-signal perturbation to (15), eliminating the steady-state values, the output function can be expressed as

$$\hat{v}_{\mathrm{o}}\left(T_k\right) = \mathbf{C}\hat{\boldsymbol{x}}_{\mathrm{s}}\left(T_k\right) \tag{42}$$

E. Z Transform

After z transform of (41) and (42), the transfer function from $\hat{f}_{\mathrm{sa\_c}}^{*}$ to $\hat{v}_{\mathrm{o}}^{*}$, $G_{v f\mathrm{sa\_c}}(z)$, can be expressed as

$$G_{vf_{\mathrm{sa\_c}}}(z) = \frac{\hat{v}_{\mathrm{o}}(z)}{\hat{f}_{\mathrm{sa\_c}}(z)} = \mathbf{C}\left(\mathbf{M}_{\mathrm{r}}z - \boldsymbol{\Phi}\right)^{-1}\left(-T_{\mathrm{sa}}^{\,2}\right)\boldsymbol{\Psi}z \tag{43}$$

where $\hat{f}_{\mathrm{sa\_c}}^{*}$ and $\hat{v}_{\mathrm{o}}^{*}$ are the sampling signals of $\hat{f}_{\mathrm{sa\_c}}$ and $\hat{v}_{\mathrm{o}}$ respectively.

Considering that the sampling frequency is a virtual signal that is unmeasurable, $G_{v f\mathrm{sa\_c}}(z)$ cannot be measured directly. Therefore, the transfer function from the modulation signal to output voltage is measured as a whole.

Furthermore, converting (43) from z-domain to s-domain and combining with (38), the transfer function from the modulation signal to output voltage can be obtained as

$$G_{\mathrm{vm\_dis\_const}}(s) = 2K_{\mathrm{VCO}}G_{vf_{\mathrm{sa\_c}}}(z)\Big|_{z = e^{sT_{\mathrm{sa}}}} \tag{44}$$

III. SMALL-SIGNAL MODELING OF VOLTAGE-CONTROLLED OSCILLATOR

It is worth noting that the derivations given in Section II are based on the assumption that VCO is a constant gain. However, the nonlinearity of VCO also has a significant effect on the model. In this section, the accurate small-signal model of VCO will be deduced.

The VCO circuit and the key waveforms are shown in Fig. 5(a) and Fig. 5(b) respectively [13], where A_1 is the voltage-controlled current source, A_2 is the comparator, A_3 is the one-shot monostable multivibrator and A_4 is the *D* flip-flop. As seen in Fig. 5(a), the modulation signal v_{m} generates i_{c} to charge the capacitor C_{fs}. When the capacitor voltage v_{Cfs} reaches the maximum value V_{cp}, A_2 outputs a pulse signal v_{p1} to trigger A_3 which generates v_{p2} to turn on the switch Q_{fs}, making v_{Cfs} drop to zero immediately. After that, v_{Cfs} rises from zero again and then starts the operation of the next charging cycle. The outputs of A_4, denoted as $Q_{\mathrm{gs\_p}}$ and $Q_{\mathrm{gs\_n}}$, are complementary square waves, which are used as the driving signals for positive and negative half period respectively. By controlling v_{m} to regulate i_{c}, changing the charging speed of C_{fs}, the switching frequency is modulated accordingly.

Applying small-signal perturbation $\hat{v}_{\mathrm{m}}$ to the modulation signal, we have

$$v_{\mathrm{m}}(t) = V_{\mathrm{m}} + \hat{v}_{\mathrm{m}}(t) \tag{45}$$

where V_{m} is the dc value.

The integral form of the voltage-ampere characteristics equation of C_{fs} in the kth charging period can be expressed as

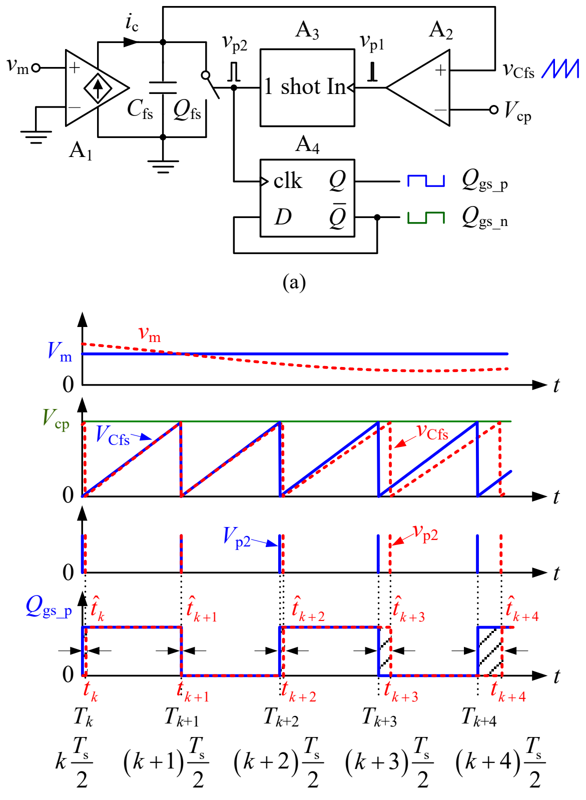

Fig. 5. The circuit diagram and key waveforms of VCO. (a) Circuit diagram; (b) Key waveforms before and after perturbation.

$$V_{\rm cp}=\frac{1}{C_{\rm fs}}\int_{t_k}^{t_{k+1}} i_{\rm c}(t)dt=\frac{1}{C_{\rm fs}}\int_{t_k}^{t_{k+1}} g v_{\rm m}(t)dt \tag{46}$$

where g is the coefficient of the voltage-controlled current source A_1.

Imposing small-signal perturbation into (46), we obtain

$$\begin{aligned} V_{\rm cp} &= \frac{g}{C_{\rm fs}}\int_{T_k+\hat{t}_k}^{T_{k+1}+\hat{t}_{k+1}}\left[V_{\rm m}+\hat{v}_{\rm m}(t)\right]dt \\ &\approx \frac{g}{C_{\rm fs}}V_{\rm m}\left(T_{k+1}+\hat{t}_{k+1}-T_k-\hat{t}_k\right)+\frac{g}{C_{\rm fs}}\int_{T_k}^{T_{k+1}}\hat{v}_{\rm m}(t)dt \end{aligned} \tag{47}$$

Eliminating the steady-state values of (47) and upon rearrangement, we have

$$\hat{t}_{{\rm sa}\_k}=\hat{t}_{k+1}-\hat{t}_k=-\frac{1}{V_{\rm m}}\int_{T_{k+1}-T_{\rm sa}}^{T_{k+1}}\hat{v}_{\rm m}(t)dt \tag{48}$$

Substituting (37) and (39) into (48), we obtain

$$\hat{f}_{{\rm sa}\_k}=2K_{\rm VCO}\frac{1}{T_{\rm sa}}\int_{T_{k+1}-T_{\rm sa}}^{T_{k+1}}\hat{v}_{\rm m}(t)dt \tag{49}$$

For notation simplification, the periodic average of $\hat{v}_{\rm m}$ defined as $\langle\hat{v}_{\rm m}\rangle_{T_{\rm sa}}$, where the period is $T_{\rm sa}$, is expressed as

$$\langle\hat{v}_{\rm m}(t)\rangle_{T_{\rm sa}}=\frac{1}{T_{\rm sa}}\int_{t-T_{\rm sa}}^{t}\hat{v}_{\rm m}(\tau)d\tau \tag{50}$$

Substituting (50) into (49) yields

$$\hat{f}_{{\rm sa}\_k}=2K_{\rm VCO}\langle\hat{v}_{\rm m}(T_{k+1})\rangle_{T_{\rm sa}} \tag{51}$$

According to Fig. 5, the charging current $i_{\rm c}$ of the capacitor $C_{\rm fs}$ changes in real-time with $v_{\rm m}$. Only when $v_{\rm Cfs}$ reaches $V_{\rm cp}$, $Q_{\rm gs\_p}$ and $Q_{\rm gs\_n}$ are flipped, meaning that $t_{{\rm sa}\_k}$ should be determined at the ending instant of the period. Therefore, $\hat{t}_{{\rm sa}\_k}$ and $\hat{f}_{{\rm sa}\_k}$ should occur at T_{k+1}. As shown in Fig. 6, $\hat{t}_{{\rm sa}\_k}$ and $\hat{f}_{{\rm sa}\_k}$ of every sampling cycle constitute the impulse trains respectively, which can be expressed as

$$\hat{t}_{\rm sa}(t)=\sum_{k=0}^{+\infty}\hat{t}_{{\rm sa}\_k}\delta(t-T_{k+1}) \tag{52}$$

$$\hat{f}_{\rm sa}(t)=\sum_{k=0}^{+\infty}\hat{f}_{{\rm sa}\_k}\delta(t-T_{k+1}) \tag{53}$$

Substituting (51) into (53) leads to

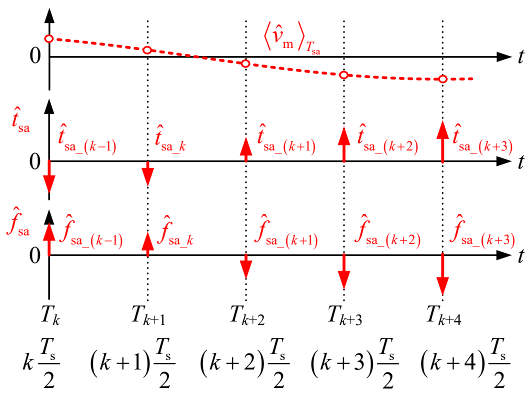

Fig. 6. The perturbation waveforms of VCO.

$$\hat{f}_{\rm sa}(t)=2K_{\rm VCO}\langle\hat{v}_{\rm m}(t)\rangle_{T_{\rm sa}}^{*} \tag{54}$$

where $\langle\hat{v}_{\rm m}\rangle_{T_{\rm sa}}^{*}$ is the sampling signal of $\langle\hat{v}_{\rm m}\rangle_{T_{\rm sa}}$, which can be written as

$$\langle\hat{v}_{\rm m}(t)\rangle_{T_{\rm sa}}^{*}=\langle\hat{v}_{\rm m}(t)\rangle_{T_{\rm sa}}\sum_{k=0}^{+\infty}\delta(t-T_{k+1}) \tag{55}$$

Furthermore, taking the Laplace transform of (50), we obtain

$$\begin{aligned} \langle\hat{v}_{\rm m}(s)\rangle_{T_{\rm sa}} &= \int_{0\_}^{+\infty}\left[\frac{1}{T_{\rm sa}}\int_{t-T_{\rm sa}}^{t}\hat{v}_{\rm m}(\tau)d\tau\right]e^{-st}dt \\ &= \frac{1}{T_{\rm sa}}\int_{0\_}^{+\infty}\left[\int_{0\_}^{t}\hat{v}_{\rm m}(\tau)d\tau-\int_{0\_}^{t-T_{\rm sa}}\hat{v}_{\rm m}(\tau)d\tau\right]e^{-st}dt \\ &= \frac{1}{T_{\rm sa}}\left\{\frac{1}{s}\hat{v}_{\rm m}(s)-\int_{0\_-T_{\rm sa}}^{+\infty}\left[\int_{0\_}^{t'}\hat{v}_{\rm m}(\tau)d\tau\right]e^{-s(t'+T_{\rm sa})}d(t'+T_{\rm sa})\right\} \\ &= \frac{1}{T_{\rm sa}}\left\{\frac{1}{s}\hat{v}_{\rm m}(s)-e^{-sT_{\rm sa}}\int_{0\_}^{+\infty}\left[\int_{0\_}^{t'}\hat{v}_{\rm m}(\tau)d\tau\right]e^{-st'}dt'\right\} \\ &= \frac{1-e^{-sT_{\rm sa}}}{sT_{\rm sa}}\hat{v}_{\rm m}(s) \end{aligned} \tag{56}$$

From (56), the transfer function from $\hat{v}_{\rm m}$ to $\langle\hat{v}_{\rm m}\rangle_{T_{\rm sa}}$, named as $G_{\rm av}(s)$, is expressed as

$$G_{\rm av}(s)=\frac{\langle\hat{v}_{\rm m}(s)\rangle_{T_{\rm sa}}}{\hat{v}_{\rm m}(s)}=\frac{1-e^{-sT_{\rm sa}}}{sT_{\rm sa}} \tag{57}$$

According to (54) and (57), the frequency domain characteristics of VCO can be mainly determined by $G_{\rm av}(s)$. Fig. 7 gives the bode diagram of $G_{\rm av}(s)$. Here, we observe that for the low-frequency range, i.e., frequencies much lower than the switching frequency, $G_{\rm av}$ is a constant. Thus, VCO can be treated as a constant gain in the low-frequency region. Besides, as the perturbation frequency increases, the magnitude of $G_{\rm av}$ decreases and the phase of it lags, which significantly influences the small-signal model of LLC resonant converter in the high-frequency region. Consequently, the nonlinearity of VCO should be incorporated in modeling.

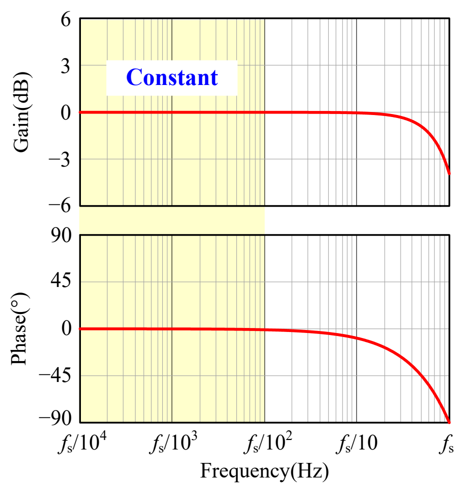

Fig. 7. Bode diagram of $G_{\rm av}(s)$.

Moreover, from (53), the small-signal component $\hat{f}_{sa\_k}$ can be expressed as

$$\hat{f}_{sa\_k} = \hat{f}_{sa}\left(T_{k+1}\right) \tag{58}$$

Substituting (37) and (58) into (34), the linearized difference equation of $\hat{\boldsymbol{x}}_s$ and $\hat{f}_{sa}$ is

$$\mathbf{M}_r \hat{\boldsymbol{x}}_s\left(T_{k+1}\right) = \mathbf{\Phi}\hat{\boldsymbol{x}}_s\left(T_k\right) - T_{sa}{}^2 \mathbf{\Psi}\hat{f}_{sa}\left(T_{k+1}\right) \tag{59}$$

After z transform of (42) and (59), the transfer function from $\hat{f}_{sa}$ to $\hat{v}_o^*$, $G_{vfsa}(z)$, can be expressed as

$$G_{vf_{sa}}\left(z\right) = \frac{\hat{v}_o\left(z\right)}{\hat{f}_{sa}\left(z\right)} = \mathbf{C}\left(\mathbf{M}_r z - \mathbf{\Phi}\right)^{-1}\left(-T_{sa}{}^2\right)\mathbf{\Psi} z \tag{60}$$

It should be noted that $G_{vfsa}(z)$ is the same as $G_{vfsa\_c}(z)$. Thus, $G_{vm\_dis\_const}(s)$ can be rewritten as

$$G_{vm\_dis\_const}\left(s\right) = 2K_{VCO} G_{vf_{sa}}\left(z\right)\Big|_{z=e^{sT_{sa}}} \tag{61}$$

According to the analysis above, Fig. 8 shows the control block diagram of LLC resonant converter, where v_e is the error signal and $\hat{v}_m^*$ is the sampling signal of $\hat{v}_m$. As seen, considering the nonlinearity of VCO, the transfer function from the modulation signal to output voltage is

$$G_{vm\_dis\_VCO}\left(s\right) = G_{av}\left(z\right)\cdot 2K_{VCO}\cdot G_{vf_{sa}}\left(z\right)\Big|_{z=e^{sT_{sa}}} \tag{62}$$

From Fig. 1 and Fig. 8, the output capacitor C_o and the feedback controller G_c behave as the low-pass filter, attenuating the high frequency components of the output voltage sufficiently. Assume that v_m is harmonic free, i.e., v_m contains only the single frequency perturbation ω_p. According to Shannon sampling theorem, we have

$$\begin{aligned} G_{av}\left(z\right)\Big|_{z=e^{sT_{sa}}} &= \frac{\left\langle \hat{v}_m\left(s\right)\right\rangle_{T_{sa}}^*}{\hat{v}_m^*\left(s\right)}\Bigg|_{s=j\omega_p} \\ &= \frac{\left\langle \hat{v}_m\left(j\omega_p\right)\right\rangle_{T_{sa}}^*}{\hat{v}_m^*\left(j\omega_p\right)} = \frac{\left\langle \hat{v}_m\left(j\omega_p\right)\right\rangle_{T_{sa}}\Big/T_{sa}}{\hat{v}_m\left(j\omega_p\right)\Big/T_{sa}} \\ &= \frac{\left\langle \hat{v}_m\left(s\right)\right\rangle_{T_{sa}}}{\hat{v}_m\left(s\right)} = G_{av}\left(s\right) \end{aligned} \tag{63}$$

Substituting (63) into (62) yields

$$G_{vm\_dis\_VCO}\left(s\right) = G_{av}\left(s\right)\cdot 2K_{VCO}\cdot G_{vf_{sa}}\left(z\right)\Big|_{z=e^{sT_{sa}}} \tag{64}$$

IV. Simulation Verification

To verify the effectiveness of the proposed discrete-time model of LLC resonant converter, the SIMPLIS simulation tool is used to measure the transfer function from the modulation signal to output voltage by sample-and-hold scheme [14]. The circuit parameters are listed as follows: P_o = 500 W, V_o = 48 V, f_r = 100 kHz, L_m = 200 μH, L_r = 40 μH, C_r = 62.5 nF, C_o = 100 μF, N = 24:6. Fig. 9 gives the simulation and the theoretical results. As seen, based on the assumption that VCO is a constant gain, $G_{vm\_dis\_const}(s)$ tends to over-estimate the phase margin in the high-frequency region and hence offers inaccurate stability information. Considering the nonlinearity of VCO, $G_{vm\_dis\_VCO}(s)$ is in very good agreement with the simulation results up to the switching frequency, verifying the accuracy of the proposed model.

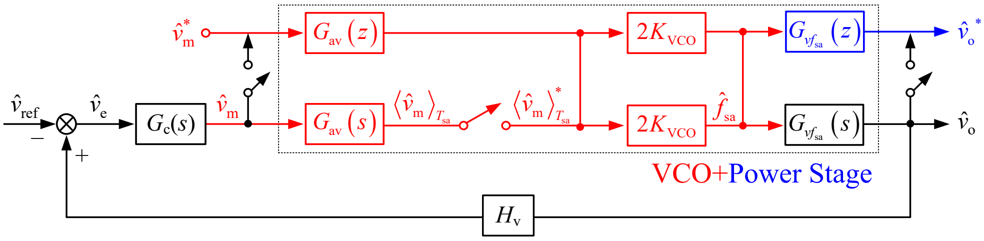

Fig. 8. Control block diagram of LLC resonant converter.

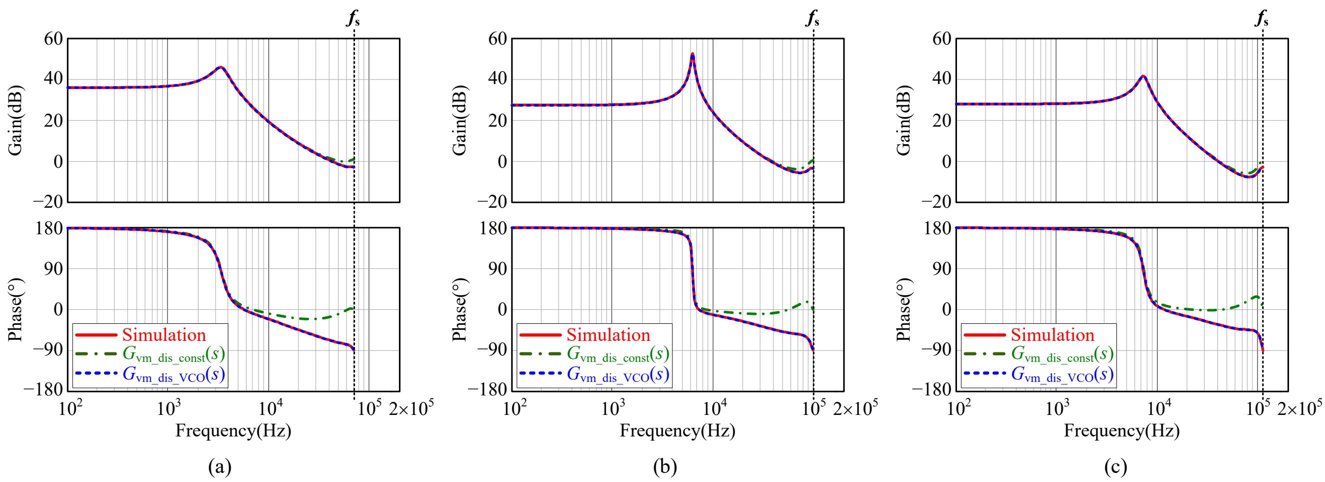

Fig. 9. Bode diagrams of the modulation signal to output voltage transfer function of LLC resonant converter by simulation and theoretical results. (a) V_{in} = 300V, f_s = 0.7f_r; (b) V_{in} = 383V, f_s = 0.99f_r; (c) V_{in} = 400V, f_s = 1.1f_r.

V. Conclusions

In this paper, a discrete-time domain model of the power stage of LLC resonant converter has been presented by exploiting the half-cycle symmetry for simplifying the analysis. The accurate small-signal model of VCO is then deduced, capturing the nonlinear characteristics. Combining VCO with the power stage, the transfer function from the modulation signal to output voltage is further derived. The corresponding block diagram of the proposed model is also illustrated, exhibiting very concise and simple form. Finally, simulation results verify the validity of the proposed model. Compared with the model where VCO is treated as a constant gain, the proposed model considering the nonlinearity of VCO can better predict the small-signal properties of LLC resonant converter, which is accurate up to the switching frequency.

References

[1] G. Chen, L. Chen, Y. Deng, K. Wang and X. Qing, "Topology-reconfigurable fault-tolerant LLC converter with high reliability and low cost for more electric aircraft," *IEEE Trans. Power Electron*., vol. 34, no. 3, pp. 2479–2493, March. 2019.

[2] M. H. Ahmed, A. Nabih, F. C. Lee and Q. Li, "Low-loss integrated inductor and transformer structure and application in regulated LLC converter for 48-V bus converter," *IEEE J. Emerg. Sel. Topics Power Electron*., vol. 8, no. 1, pp. 589–600, March. 2020.

[3] Y. Shen, W. Zhao, Z. Chen and C. Cai, "Full-bridge LLC resonant converter with series-parallel connected transformers for electric vehicle on-board charger," *IEEE Access*, vol. 6, pp. 13490−13500, 2018.

[4] C. Chang, C. Cheng and H. Cheng, "Modeling and design of the LLC resonant converter used as a solar-array simulator," *IEEE J. Emerg. Sel. Topics Power Electron*., vol. 2, no. 4, pp. 833−841, Dec. 2014.

[5] R. D. Middlebrook and S. Cuk, "A general unified approach to modelling switching-converter power stages," in *Proc. IEEE Power Electron. Spec. Conf*., 1976, pp. 18−34.

[6] E. X. Yang, F. C. Lee and M. M. Jovanovic, "Small-signal modeling of series and parallel resonant converters," in *Proc. IEEE Appl. Power Electron. Conf. Expo*., 1992, pp. 785−792.

[7] E. X. Yang, F. C. Lee and M. M. Jovanovic, "Small-signal modeling of LCC resonant converter," in *Proc. IEEE Power Electron. Spec. Conf*., 1992, pp. 941−948.

[8] C. Chang, E. Chang, C. Cheng, H. Cheng and S. Lin, "Small signal modeling of LLC resonant converters based on extended describing function," in *Proc. Int. Symp. Comput. Consum. Control*, 2012, pp. 365−368.

[9] Y. -H. Hsieh and F. C. Lee, "Accurate small-signal model for LLC resonant converters," in *Proc. IEEE Energy Convers. Congr. Expo*., 2019, pp. 660−665.

[10] V. Vorperian and S. Cuk, "Small signal analysis of resonant converters," in *Proc. IEEE Power Electron. Spec. Conf*., 1983, pp. 269−282.

[11] G. C. Verghese, M. E. Elbuluk and J. G. Kassakian, "A general approach to sampled-data modeling for power electronic circuits," *IEEE Trans. Power Electron*., vol. 1, no. 2, pp. 76−89, April. 1986.

[12] I. Batarseh and K. Siri, "Generalized approach to the small signal modelling of dc-to-dc resonant converters," *IEEE Trans. Aerosp. Electron. Syst*., vol. 29, no. 3, pp. 894−909, July. 1993.

[13] X. Li, Y. Zhang, S. Chen, X. Zhang and Y. Tang, "Pulsewidth-modulator-based transfer function measurement method for variable frequency-controlled half- and full-bridge converters," *IEEE Trans. Power Electron*., vol. 36, no. 9, pp. 9711−9716, Sept. 2021.

[14] X. Ruan et al., "Reconsideration of loop gain and its measurement in dc-dc converters," *IEEE Trans. Power Electron*., vol. 34, no. 7, pp. 6906−6921, July. 2019.